Available online at www.sciencedirect.com
ScienceDirect
Journal of the European Ceramic Society 27 (2007) 125–130
www.elsevier.com/locate/jeurceramsoc

# Phase transformation of ultrafine rare earth oxide powders synthesized by radio frequency plasma spraying

X.L. Sun [a], A.I.Y. Tok [a,*], R. Huebner [b], F.Y.C. Boey [a]

[a] School of Materials Science and Engineering, Nanyang Technological University, 50 Nanyang Avenue, Singapore 639798, Singapore
[b] College of Nanoscale Science and Engineering, University at Albany, SUNY, 255 Fuller Road, Albany, NY 12203, USA

Received 17 December 2005; received in revised form 19 April 2006; accepted 29 April 2006
Available online 16 June 2006

**Abstract**

Inductively coupled radio frequency plasma spraying was used to prepare ultrafine powders of $Sm_2O_3$, $Dy_2O_3$, and $Lu_2O_3$. These three materials were studied because they are effective dopants in multi-layer ceramic capacitors (MLCC) to improve lifetime. The as-sprayed powders consist of both micron-sized mono-dispersed spherical particles and nano-sized particles in various shapes. In addition to the spheroidization effect, plasma treatment leads to an increase of the monoclinic phase fraction associated with a corresponding decrease of the amount of the cubic phase. The degree of this phase change was found to depend sensitively on the sprayed oxides, decreasing with increasing atomic number of the rare earth element, which is associated with their thermodynamic stability. Furthermore, the monoclinic high-temperature equilibrium phase induced by plasma treatment remains stable at room temperature and even during annealing at a temperature of 900 °C.


*Keywords:* Plasma spraying; Phase transformation; $Sm_2O_3$; $Dy_2O_3$; $Lu_2O_3$

## 1. Introduction

Rare earth oxides have the greatest, most negative, standard free energies of formation compared with any other oxides, accounting for their exceptional thermodynamic stability.[1] These oxides occur in several oxidation states of which the trivalent is the most common. The solid state chemistry of rare earth atoms in combination with oxygen is primarily dependent upon their electronic configuration and ionic size. As electrons are added to the 4f orbital, the increasing nuclear charge is effectively shielded by the outer $5d^1$ and $6s^2$ valence electrons. This makes the valency hold favorably in a trivalent state for most rare earths whose energy varies gradually across the series.[2] Generally, rare earth sesquioxides ($R_2O_3$) crystallize in five different structures, named A, B, C, H, and X. The A-type (hexagonal) structure can be described in space group *P*32/*m* with 1 formula $R_2O_3$/unit cell. The B-type (monoclinic) structure is of space group *C*2/*m* with 6 formulas/unit cell, and the C-type (cubic) structure is described in space group $Ia\bar{3}$, containing 16 $R_2O_3$ molecules/unit cell. The H-type (hexagonal) and X-type (cubic) structures are found only at temperatures above 2000 K. The A-type and the closely related B-type structures are adopted by the lighter rare earths, whereas the C-type is found for the heavier rare earths and similarly sized Yttrium.[3] With increasing atomic number, the ionic radii of rare earth decrease steadily throughout the series, the thermodynamic stability of the rare earth sesquioxides increase, and the stability area of the cubic C-type phase is considerably expanded.

Due to their unique properties, numerous functional materials based on rare earth oxides have been developed in a variety of fields, including phosphors,[4] catalysts,[5] and fuel cells,[6,7] etc. Some of these applications have reached the technological maturity, which is associated with large scale industrial consumption of the rare earth oxides.

Since the 1980s, ultrafine rare earth oxide particles ranging from nanometer to sub-micrometer scale have attracted much concern due to their remarkably different physical and chemical properties from those of bulk materials. These extraordinary properties are attributed to quantum size and surface effects.[8] Besides the particle size, in some applications, such as phosphors, the particle shape and the agglomeration degree are of great importance. Non-agglomerated spherical particles are pre-

* Corresponding author.
*E-mail address:* miytok@ntu.edu.sg (A.I.Y. Tok).

0955-2219/$ – see front matter © 2006 Elsevier Ltd. All rights reserved.
doi:10.1016/j.jeurceramsoc.2006.04.172

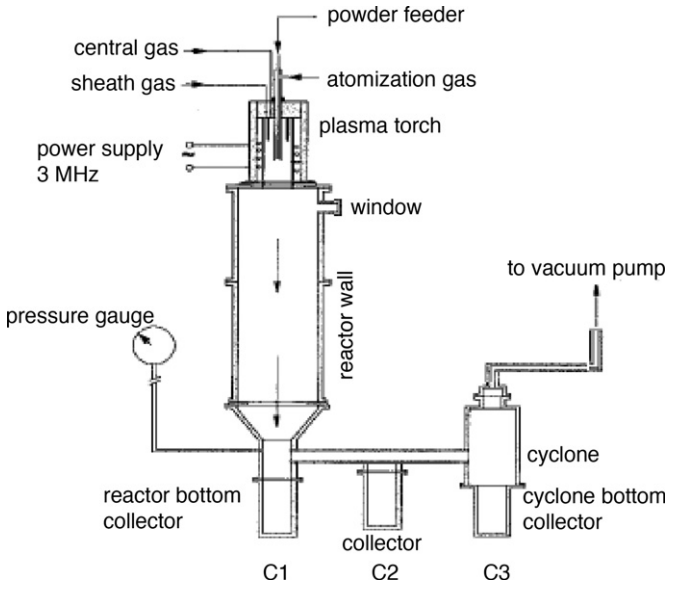


Fig. 1. Inductively coupled RF plasma spraying system.

ferred as such a shape offers the most efficient packing and smallest surface-to-volume ratio. Due to the employment of new processes for ultrafine powder preparation[9,10] and the application of high-resolution transmission electron microscopy (HRTEM) for characterization,[11] there has been substantial progress in both fundamental and applied research for rare earth materials within the last 10 years. Currently, there are, however, still some limitations in conjunction with the powder preparation processes, e.g. contamination, complexity in procedure, or low throughput.

Inductively coupled radio frequency plasma spraying, powered by high-frequency oscillating electrical current, performs an important role in fine powder manufacture.[12] Its main advantages include minimum contamination, high energy density, spheroidization effect, and flexibility in pressure and atmosphere.[13] In this paper, ultrafine powders of rare earth sesquioxides $Sm_2O_3$, $Dy_2O_3$, and $Lu_2O_3$ were prepared using this technique. The particle size distribution, morphology and phase compositions of the as-sprayed powders were studied.

## 2. Experimental procedure

### 2.1. Equipment

The powder processing was carried out using a 35 kW Tekna Plasma System with RF plasma torch (PL-35) operating at 3 MHz (Fig. 1). The installation comprises a RF power supply, a plasma torch, plasma gas control system, vacuum pumping system, water cooling system, a powder feeder, and three powder collection chambers. Argon was used as plasma central gas, sheath gas, and feeding carrier gas. The corresponding flow rates were fixed at 20, 50, and 6 slpm (standard liters/min), respectively. Spraying was done at a power input of 18 kW and a chamber pressure of $5.332 \times 10^4$ Pa. Pure $Sm_2O_3$, $Dy_2O_3$, and $Lu_2O_3$ powders (from AMR Technologies Inc., purity 99.5 wt.%) were used as starting materials. With a constant rate, this raw material was fed by a pair of screw conveyers into the powder feeder and carried by argon gas, flowing axially into the center of the plasma plume through the probe. After plasma treatment, the material was quenched with extremely high speed and was subsequently collected by cyclone into three chambers. The chambers enabled the collection of particles with different size ranges. From chamber 1 (C1), chamber 2 (C2) to chamber 3 (C3), the collected powders have a decreasing tendency in particle size.

### 2.2. Characterization

The particle size and morphology of the sprayed powders were studied using Fritsh Analysette 22 Laser Particle Sizer (for raw materials, sprayed C1 and C2 powders), Malvern Zetasizer Nano ZS (for sprayed C3 powders), scanning electron microscopy (SEM, JEOL JSM 6340F) and transmission electron microscopy (TEM, JEOL JEM 2010). For phase analysis of the processed polycrystalline powders, X-ray diffraction (XRD) experiments were done in Bragg–Brentano geometry employing a Shimadzu 6000 diffractometer with Cu Kα radiation ($\lambda = 1.5418$ Å). To determine the lattice parameters as well as the quantitative phase composition, further evaluation of the diffraction patterns by means of the Rietveld method was carried out using the TOPAS software.[14] Differential scanning calorimeter (NETZSCH DSC 404) was employed to determine the phase transformation temperature of sprayed powder.

## 3. Results

$Sm_2O_3$, $Dy_2O_3$, and $Lu_2O_3$ raw material powders used were mainly in the micron size, with a wide particle size distribution (shown in Fig. 2(a)). Fig. 3 shows SEM micrographs of the different rare earth oxides powders before and after plasma spraying. As indicated for $Dy_2O_3$ in Fig. 3(a), particles of the raw materials have dimensions in the micron range and are of irregular shape. Plasma spraying, however, changes size and morphology. Powder collected in chambers C1 and C2 consists mainly of micron-sized spheres with smooth surfaces, suggesting a melting history (Fig. 3(b and c)). Their particle size distribution shown in Fig. 2(b and c) indicates that the sizes of $Sm_2O_3$ and $Dy_2O_3$ sprayed powders from C1 and C2 decrease as compared with raw materials, while that of $Lu_2O_3$ has little change. The presence of a small amount of irregularly shaped large particles can be explained by insufficient heat treatment and, thus, incomplete melting of the raw material. From Fig. 2(d) it can be seen that the particle size of $Dy_2O_3$ powder decreases after spraying. Additionally, the sprayed $Dy_2O_3$ powder collected in chambers C1 (Fig. 3(b)) and C2 (Fig. 3(c)) contains a small fraction of nano-sized particles which can be deduced from the light-gray clusters visible in the background of the micrographs. Taking Fig. 3(e) into consideration, it can be deduced that the fraction of nano-sized particles increases in the order C1 → C2 → C3. Comparing the morphology of different rare earth oxide particles collected in the same chamber indicates another tendency. With increasing atomic number of the rare earth metal, the fraction of the micro-sized spherical particles increases and, accordingly, that one of the nano-sized particles decreases, as can be seen for the C3 powders in Fig. 3(d–f).

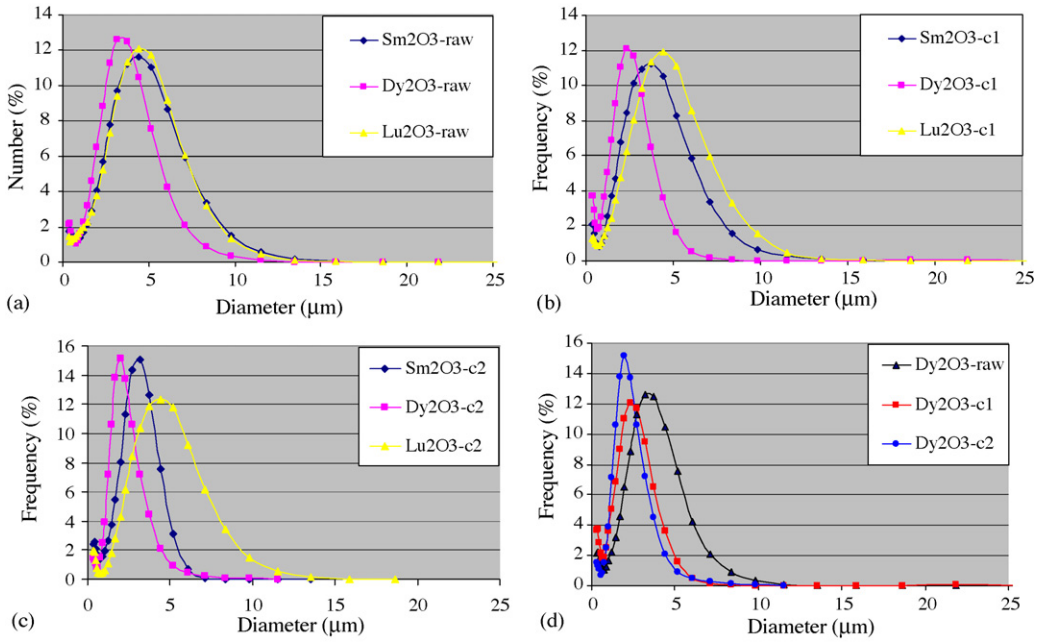


Fig. 2. Particle size distribution of raw materials and sprayed powders:s (a) raw material; (b) sprayed C1 powders; (c) sprayed C2 powders; (d) $Dy_2O_3$ raw material and sprayed powders.

After separating micro- and nano-sized particles of C3 powders by ultrasonic vibration, the nano-sized particles were measured by laser nano-particle sizer. The results in Fig. 4 suggest that they have an average particle size around 50 nm (due to agglomeration, nano-particles below 30 nm, which can be observed under TEM, were not detected by the laser). TEM micrographs in Fig. 5 reveal that instead of being totally spherical, some of the nano-particles are of elliptical or irregular shape (Fig. 5(a)). Furthermore, high resolution TEM pictures (Fig. 5 (b)) show that the nano-particles are single crystalline. In some cases, there is a small amount of amorphous phase connecting the single crystallites (Fig. 5(b)). The amorphous phase seems to be the result from extremely high speed cooling of the vaporized material.

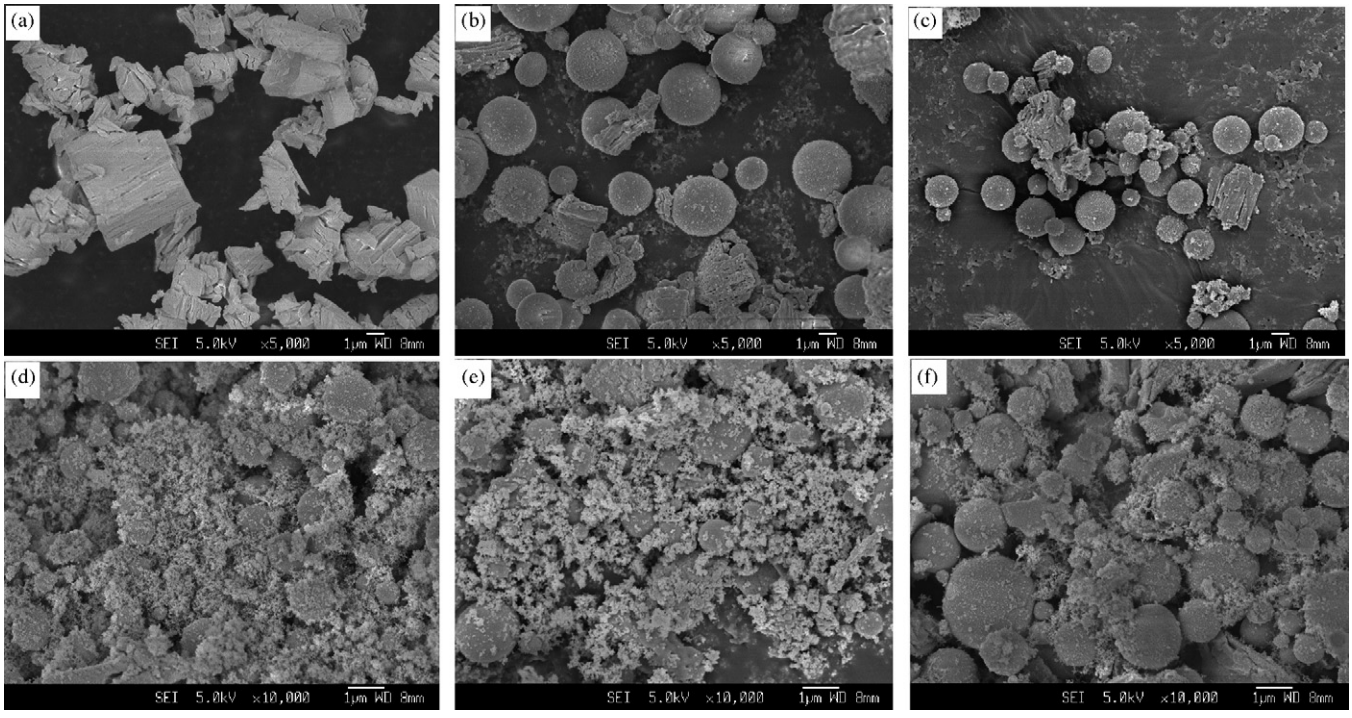


Fig. 3. SEM micrographs of different rare earth oxide powders before and after RF plasma spraying: (a) $Dy_2O_3$ raw material; (b and c) sprayed $Dy_2O_3$ powder collected in chamber C1 and C2; (d–f) $Sm_2O_3$, $Dy_2O_3$, and $Lu_2O_3$ powder collected in chamber C3.

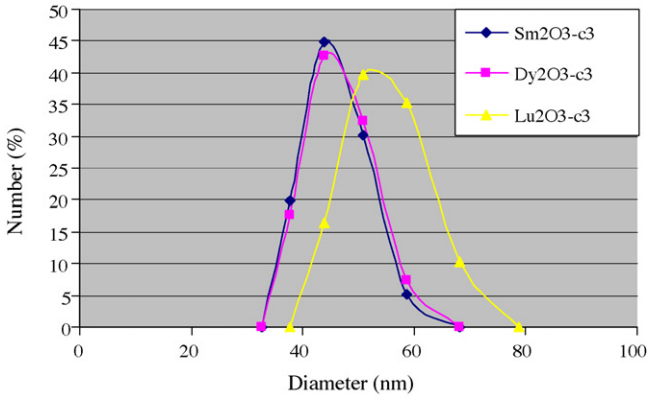


Fig. 4. Particle size distribution of sprayed C3 powders: (a) $Sm_2O_3$; (b) $Dy_2O_3$; (c) $Lu_2O_3$.

To determine the phase composition of the powders before and after spraying as well as the associated lattice parameters of the unit cells, XRD patterns were collected and analyzed by Rietveld refinement. $Sm_2O_3$ raw material consists mainly of the monoclinic B-type phase (JCPDS-ICDD 42-1464). Additionally, there is a small amount (7 wt.%) of the cubic C-type phase (JCPDS-ICDD 15-0813). In contrast, the raw materials of $Dy_2O_3$ and $Lu_2O_3$ only contain the cubic C-type phase (JCPDS-ICDD 22-0612 and 12-0728, respectively (Fig. 6, curve (a))). For all rare earth oxide powders, RF plasma spraying results in an increase of the fraction of the monoclinic B-type phase. Taking $Dy_2O_3$ for example (Fig. 6), it can be clearly identified that after spraying there are both cubic and monoclinic Bragg reflections in the diffraction patterns. Moreover, the monoclinic phase is more pronounced. Comparing the diffraction diagrams for the sprayed $Dy_2O_3$ powders in more detail (Fig. 6, curves (b–d)), it can be seen that there is an intensity decrease for the cubic Bragg reflections in the order C1 → C2 → C3. Consequently, the fraction of the monoclinic phase increases which is confirmed by quantitative phase analysis (Fig. 8). It should be mentioned that calcination of sprayed $Dy_2O_3$ powder collected in chamber C2 at 900 °C for 4 h does not result in a change of the phase composition. Thus, this monoclinic high-temperature equilibrium

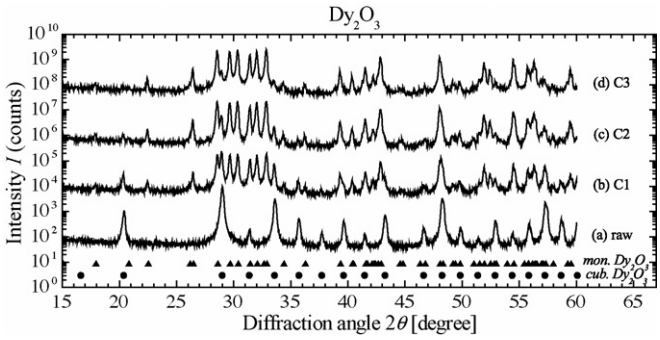


Fig. 6. (a–d) XRD patterns of $Dy_2O_3$ raw material and sprayed powders.

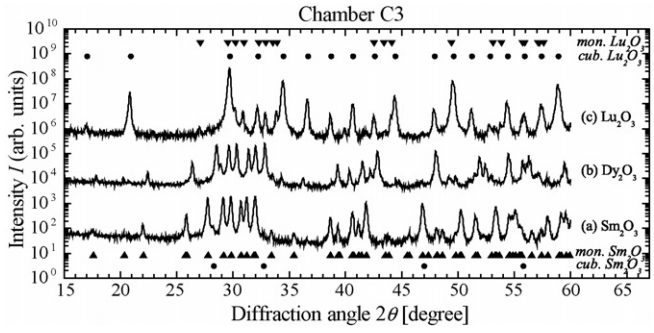


Fig. 7. (a–c) XRD patterns of $Sm_2O_3$, $Dy_2O_3$, and $Lu_2O_3$ sprayed powders from chamber C3.

phase is stable even during heat treatment at low temperatures. As in the case of $Dy_2O_3$, the fraction of the monoclinic B-type phase also increases for the other rare earth oxides during RF plasma spraying. However, the degree of the phase change is different. Comparing the diffraction patterns for $Sm_2O_3$, $Dy_2O_3$, and $Lu_2O_3$ powder collected in chamber C3 (Fig. 7), there is an intensity decrease for the monoclinic Bragg reflections and, thus, a decrease of the fraction of the B-type phase with increasing atomic number of the rare earth metal. This observation is confirmed by the results of the quantitative phase analysis (Fig. 8).

Besides the fractions of the various phases, quantitative analysis of diffraction patterns also provides the lattice parameters

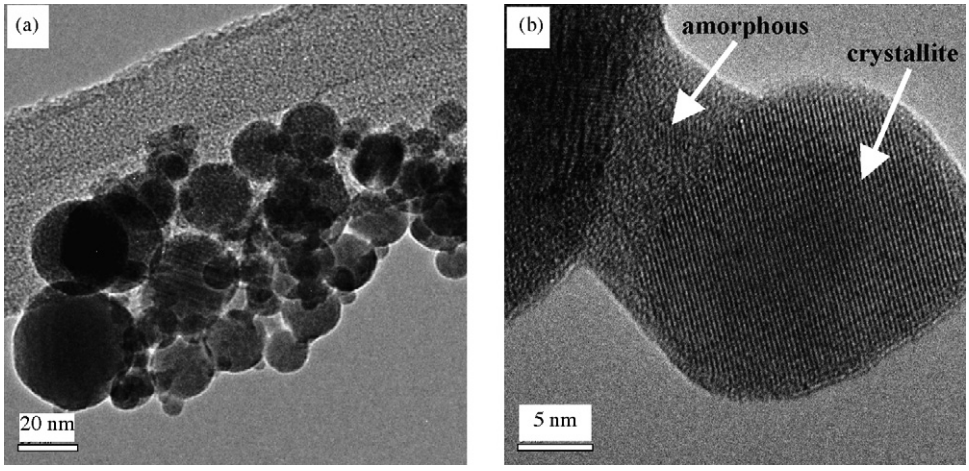


Fig. 5. (a and b) TEM micrographs of $Sm_2O_3$ nano-particles from chamber C3.

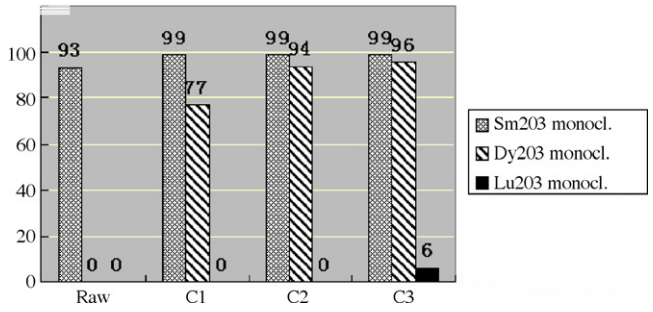


Fig. 8. Results of the quantitative phase analysis for raw and sprayed materials, whereby the fractions of the monoclinic phase are given in wt.% (as there is no reliable structure information for monoclinic $Dy_2O_3$ and $Lu_2O_3$, structure data of monoclinic $Sm_2O_3$ was used for Rietveld refinement, as they have similar structure[2]).

of the corresponding unit cells. For sprayed $Sm_2O_3$, $Dy_2O_3$, and $Lu_2O_3$ powder from chamber C3, they are listed together with the associated unit cell volume $V$ as well as the equivalent volume $V_{R_2O_3}$ of one molecular unit $R_2O_3$ in Table 1. As the fractions of cubic $Sm_2O_3$, cubic $Dy_2O_3$, and monoclinic $Lu_2O_3$ are very small (Fig. 8), the corresponding lattice parameters were determined with high uncertainties resulting in large errors. Concerning the cubic phase, the lattice parameter $a$ and, thus, the associated unit cell volume $V$ decrease with increasing atomic number of the rare earth metal. This result can be explained by the lanthanide contraction effect and is in accordance with the shift of the cubic Bragg reflections to higher diffraction angles (Fig. 7), which can be observed best for the 2 2 2 reflection ($Sm_2O_3$: $2\theta = 28.2°$, $Dy_2O_3$: $2\theta = 28.9°$, $Lu_2O_3$: $2\theta = 29.7°$). A similar tendency is observed for the monoclinic phase. With decreasing lattice parameters $a$, $b$, $c$ and increasing monoclinic angle $\beta$, the unit cell volume decreases in the order $Sm_2O_3 \rightarrow Dy_2O_3 \rightarrow Lu_2O_3$. In the case of the cubic phase, the calculated unit cell volumes are in good accordance with already published values ($V_{Sm_2O_3} = 1304.89\,Å^3$,[15] $V_{Dy_2O_3} = 1214.97(24)\,Å^3$,[16] $V_{Lu_2O_3} = 1121.95\,Å^3$[17]) whereas for the monoclinic cell, there are slight differences,[18,19] which might be caused by trace impurities in the raw material.

Table 1
Lattice parameters of sprayed $Sm_2O_3$, $Dy_2O_3$, and $Lu_2O_3$ powders from chamber C3

| | $Sm_2O_3$ | $Dy_2O_3$ | $Lu_2O_3$ |
|---|---|---|---|
| Monoclinic | | | |
| $a$ (Å) | 14.1803(7) | 13.9498(9) | 13.7486(26) |
| $b$ (Å) | 3.6275(2) | 3.5181(3) | 3.4050(7) |
| $c$ (Å) | 8.8558(5) | 8.6616(6) | 8.4420(19) |
| $\beta$ (°) | 100.043(4) | 100.169(5) | 100.281(19) |
| $V$ (Å$^3$) | 448.55(4) | 418.40(5) | 388.86(14) |
| $V_{R_2O_3,mon}$ (Å$^3$) | 74.759(7) | 69.734(8) | 64.809(23) |
| Cubic | | | |
| $a$ (Å) | 10.9301(69) | 10.6655(45) | 10.3933(2) |
| $V$ (Å$^3$) | 1305.80(247) | 1213.22(152) | 1122.67(7) |
| $V_{R_2O_3,cub}$ (Å$^3$) | 81.612(154) | 75.826(95) | 70.167(4) |

## 4. Discussion

The wide particle size distribution of the sprayed powders observed in the SEM micrographs in Fig. 3 can be attributed to two factors. The first one is the different degree of heat treatment arising from the thermal gradient in the plasma plume and a different residence time of the injected particles therein. When fed downstream into the plasma plume, each particle takes a certain trajectory path. All these paths form a cone shape trajectory zone in the plasma plume. In principle, injected particles undergo heating, flash melting, and subsequent evaporation in the plume due to the high enthalpy. After leaving the plasma plume tail, the vaporized material is quenched at a rate up to $10^5$ °C/s[13] and condenses into nano-sized particles. Generally, the whole process takes about 10 ms depending on the size of the plume, the trajectory, and the velocity of the particles in the plasma.[20] Undoubtedly, increasing the energy input promotes further melting and evaporation. However, under the same process conditions, the degree of heat treatment for each particle can be different. Those particles having small trajectory angles travel through almost the whole plume length. They have a longer residence time in the plume and undergo a higher degree of heat treatment, resulting in more evaporation and nano-sized particles. On the contrary, particles with large trajectory angles have short residence time and get insufficient heat input, thus maintain an irregular shape as the raw material. The second factor influencing the as-sprayed particle size distribution is the particle size difference within the raw powder. Due to the high thermodynamic stability of rare earth oxides, large particles vaporize only partially at the surface, while small ones are liable to vaporize totally. When cooled down, vaporized material condenses into nano-particles and melted particles become smooth micron-sized balls. Therefore, considering these two factors, a large particle size distribution is inevitable.

As already mentioned before, there are two tendencies which can be deduced from the SEM pictures in Fig. 3. Firstly, for all the three sprayed materials, the amount of irregularly shaped large particles as well as that one of micron-sized spheres decreases from chamber C1 to chamber C3, whereas the amount of nano-particles increases (Fig. 3(a–c and e)). This observation is the consequence of the classification effect of the cyclone and the collection chambers. Smaller and lighter particles tend to be carried farther and reside into chamber C3. Secondly, for all the three chambers, the amount of large micron-sized particles increases from $Sm_2O_3$ to $Lu_2O_3$, whereas the amount of nano-particles decreases (Fig. 3(d–f)). This observation may be interpreted with a different thermodynamic stability of the raw materials. From $Sm_2O_3$, $Dy_2O_3$ to $Lu_2O_3$, the melting temperature $T_m$ increases, with $Sm_2O_3$ the easiest to be melt and vaporized and $Lu_2O_3$ the hardest ($T_{m,Sm_2O_3} = 2335$ °C; $T_{m,Dy_2O_3} = 2408$ °C; $T_{m,Lu_2O_3} = 2490$ °C[2]). Consequently, using the same plasma conditions, there are less micron-sized particles and more nano-sized particles for sprayed $Sm_2O_3$ than for sprayed $Lu_2O_3$.

As in the case of the SEM investigations, two principal results are obtained from the XRD analysis. Firstly, for each of the rare earth oxides, there is an increase of the fraction of the monoclinic B-type phase after spraying. In particular, the amount of

this monoclinic phase is dependent on the collection chamber increasing in the order C1 → C2 → C3 (Figs. 6 and 8). Secondly, for a specific collection chamber, the monoclinic phase fraction of the powder varies with the sprayed oxide. It decreases with increasing atomic number of the rare earth species. This means that in the series $Sm_2O_3 \rightarrow Dy_2O_3 \rightarrow Lu_2O_3$, the probability to undergo a monoclinic-to-cubic phase change during cooling down of the material increases, which can be elucidated with a considerable expansion of the stability region of the cubic phase in this order.[3] A comparison of the SEM results with those of the XRD analysis suggests that the nano-sized particles are mainly composed of crystallites with B-type structure. However, it should be kept in mind that there are also nano-particles which do not have a monoclinic structure. $Lu_2O_3$ powder collected in chamber C2, for instance, consists of nano-particles (SEM micrograph not shown here), but only Bragg reflections of the cubic C-type phase are observable in the diffraction pattern. Furthermore, not all of the large spherical particles are cubic. $Sm_2O_3$ powder collected in chamber C2 contains a high amount of micron-sized balls, whereby the dominant phase is the monoclinic one (Fig. 8).

According to Kim and Kriven,[19] the monoclinic B-type structure is thermodynamically unstable at room temperature because the lattice is inherently strained and some rare earth atoms (R) are getting very close to each other such that strong repulsive forces are developed in the structure. Thus, the B-type structure tends to transform back into the cubic C-type structure which has larger R–R distances to release lattice strains and cation charge repulsion by maximizing the volume. This B-type to C-type transformation is displacive, involving the breaking of some R–O bonds and the reconstruction of the coordination. Thus, an energy input is required to overcome the barrier of breaking the R–O bonds in the structure. One possible way is heat treatment below the C-type to B-type transformation temperature.[21] In the present study, DSC measurements showed that the phase transformation of the sprayed $Dy_2O_3$ powder from chamber C2 begins at 943 °C, and annealing the powder at 1000 °C for 4 h induces a transformation of 88 wt.% of B-type structure back to C-type structure. Meanwhile, the morphology and particle size of annealed powder remains the same as-sprayed powder.

## 5. Conclusions

Ultrafine rare earth sesquioxides of $Sm_2O_3$, $Dy_2O_3$, and $Lu_2O_3$ were produced by inductive RF plasma spraying. Generally, the powders obtained consist of monoclinic B-type phase as well as cubic C-type phase and are characterized by a particle size distribution ranging from 5 nm to 10 μm, with micro-sized particles of spherical shape and nano-sized particles of various shapes. Besides the preparation process, the particle size distribution is influenced by the sprayed powder itself. Furthermore, it was shown that plasma treatment leads to a decrease of the cubic phase fraction and correspondingly to an increase of the monoclinic phase fraction. The strength of this phase composition change varies with the oxide powder used for spraying and can be explained by the dependence of the thermodynamic stability of both $R_2O_3$ structures on the rare earth species. According to additional experiments, the monoclinic high-temperature equilibrium phase remains stable at ambient temperature and even during annealing at 900 °C.

## References


1. Gschneidner, K. A. and Eyring, L. R., *Handbook on the Physics and Chemistry of Rare Earths*, *Vol. 3*. North-Holland, Amsterdam, 1979.
2. Adachi, G., Imanaka, N. and Kang, Z. C., *Binary Rare Earth Oxides*. Kluwer Academic Publishers, 2004.
3. Molycorp Inc., *A Lanthanide Lanthology. Part II*. Molycorp Inc., CA, USA, 1994.
4. Ronda, C. R., Jüstel, T. and Nikol, H., Rare earth phosphors: fundamentals and applications. *J. Alloys Compd.*, 1998, **275–277**, 669.
5. Forlani, O. and Rossini, S., Rare earths as catalysts for the oxidative coupling of methane to ethylene. *Mater. Chem. Phys.*, 1992, **31**(1–2), 155.
6. Tok, A. I. Y., Luo, L. H. and Boey, F. Y. C., Carbonate co-precipitation of $Gd_2O_3$-doped $CeO_2$ solid solution nano-particles. *Mater. Sci. Eng. A*, 2004, **383**, 229.
7. Tok, A. I. Y., Luo, L. H., Boey, F. Y. C. and Ng, S. H., Consolidation and properties of $Gd_{0.1}Ce_{0.9}O_{1.95}$ nano-particles for SOFC electrolytes. *J. Mater. Res.*, 2005, **21**, 119.
8. Adachi, G. and Imanaka, N., The binary rare earth oxides. *Chem. Rev.*, 1998, **98**, 1479.
9. Dupont, A., Parent, C., Le Garrec, B. and Heintz, J. M., Size and morphology control of $Y_2O_3$ nanopowders via a sol–gel route. *J. Solid State Chem.*, 2003, **171**, 152.
10. Bondioli, F., Corradi, A. B., Leonelli, C. and Manfredini, T., Nanosized $CeO_2$ powders obtained by flux method. *Mater. Res. Bull.*, 1999, **34**, 2159.
11. Lopez-Cartes, C., Perez-Omil, J. A., Pintado, J. M., Calvino, J. J, Kang, Z. C. and Eyring, L., Rare-earth oxides with fluorite-related structures: their systematic investigation using HREM images, image simulations and electron diffraction pattern simulations. *Ultramicroscopy*, 1999, **80**, 19.
12. Fridman, A. and Kennedy, L. A., *Plasma Physics and Engineering*., 2004.
13. Boulos, M. I., The inductively coupled R.F. (radio-frequency) plasma. *Pure Appl. Chem.*, 1985, **57**(9), 1321.
14. Bruker, A. X. S., *TOPAS V2.1: General Profile and Structure Analysis Software for Powder Diffraction Data—User's Manual*. Bruker AXS, Karlsruhe, Germany, 2003.
15. Bartos, A., Lieb, K. P., Uhrmacher, M. and Wiarda, D., Refinement of atomic positions in bixbyite oxides using perturbed angular correlation spectroscopy. *Acta Crystallogr.*, 1993, **B49**, 165–169.
16. Maslen, E. N., Streltsov, V. A. and Ishizawa, N., A synchrotron X-ray study of the electron density in C-type rare earth oxides. *Acta Crystallogr.*, 1996, **B52**, 414–422.
17. Marsella, L. and Fiorentini, V., Structure and stability of rare-earth and transition-metal oxides. *Phys. Rev.*, 2004, **B69**, 172103.
18. Schleid, T. and Meyer, G., Single crystals of rare earth oxides from reducing halide melts. *J. Less-Common Met.*, 1989, **149**, 73–80.
19. Kim, Y. J. and Kriven, W. M., Crystallography and microstructural studies of phase transformations in the $Dy_2O_3$ system. *J. Mater. Res.*, 1998 Oct., **13**(10).
20. Boulos, M. I., Diagnostics of thermal plasmas. In *Frontiers of Low Temperature Plasma Diagnostics III Conference*, 1999.
21. Venkatachari, K. R. and Kriven, W. M., Investigation of plasma-sprayed dysprosia coatings. *J. Am. Ceram. Soc.*, 1989, **72**(10), 2023–2026.